We are IntechOpen, the world's leading publisher of Open Access books Built by scientists, for scientists

4,800
Open access books available

122,000
International authors and editors

135M
Downloads

Our authors are among the

154
Countries delivered to

TOP 1%
most cited scientists

12.2%
Contributors from top 500 universities

WEB OF SCIENCE™

Selection of our books indexed in the Book Citation Index in Web of Science™ Core Collection (BKCI)

Interested in publishing with us?
Contact book.department@intechopen.com

Numbers displayed above are based on latest data collected.
For more information visit www.intechopen.com

10

Semiconductor Superlattice-Based Intermediate-Band Solar Cells

Michal Mruczkiewicz, Jarosław W. Kłos and Maciej Krawczyk
Faculty of Physics, Adam Mickiewicz University, Poznań
Poland

1. Introduction

The efficiency of conversion of the energy of photons into electric power is an important parameter of solar cells. Together with production costs, it will determine the demand for the photovoltaic device and its potential use (Messenger & Ventre, 2004). The design of artificial nanostructures with suitably adjusted properties allows to increase the performance of solar cells. The proposed concepts include, among others, third-generation devices such as tandem cells, hot carrier cells, impurity photovoltaic and intermediate-band cells (Green, 2003). In this chapter we discuss the theoretical model of intermediate-band solar cell (IBSC), the numerical methods of determining the band structure of heterostructures, and the latest reported experimental activities. We calculate the efficiency of IBSCs based on semiconductor superlattices. The detailed balance efficiency is studied versus structural and material parameters. By adjusting these parameters we tailor the band structure to optimize the efficiency.

The background of the concept of IBSC lies in the impurity solar cell concept proposed by (Wolf, 1960) and presented in Fig. 1. The idea was to increase the efficiency by the introduction of intermediate states within a forbidden gap of the semiconductor. This allows the absorption of low-energy photons and causes them to contribute to the generated photocurrent via two-photon absorption. However, as shown experimentally by (Guettler & Queisser, 1970), the introduction of intermediate levels via impurities will create non-radiative recombination centers and cause a degradation of the solar cell efficiency. This effect was studied theoretically by (Würfel, 1993) and (Keevers & Green, 1994), with the conclusion that the introduced impurity levels can increase the efficiency in some cases, but only marginally. However the research in this field is still active and recently the optical transition between CB and IB band in the GaN_xAs_{1-x} alloys was proved experimentally (López et al., 2011; Luque, 2011).

Another, more sophisticated approach to the concept of impurity solar cell was proposed by (Barnham & Duggan, 1990). A further discussion in (Araujo & Martí, 1995), (Luque & Martí, 2001), (Martí et al., 2006) led to the conclusion that the problems related to the impurity states in the solar cell concept might be overcome if the impurities interacted strongly enough to form an impurity band (IB). In such conditions the electron wave functions in the IB are delocalized, causing the radiative recombinations to predominate over the non-radiative ones. The efficiency of the system was described by (Luque & Martí, 1997) on the basis of the extended Shockly-Queisser model (Shockley & Queisser, 1961), the most commonly used

and described in detail in the next section. Many extended versions of the model have been developed, such as that proposed by (Navruz & Saritas, 2008) in a study of the effect of the absorption coefficient, or the model of (Lin et al., 2009), considering the carrier mobility and recombinations.

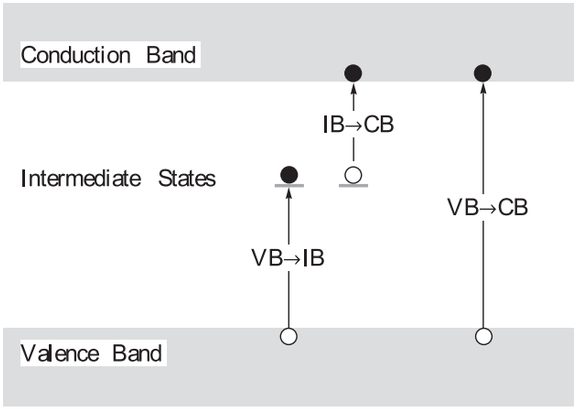

Fig. 1. Model of single-gap solar cell with impurity states introduced. Two possible ways of electron-hole creation are shown: via one-photon absorption in a transition from the valence band to the conduction band (VB→CB), and via two-photon absorption, in which the electron is excited from the valence band to the impurity state (VB→IB) by one photon, and from the impurity state to the conduction band (IB→CB) by another photon.

2. Theoretical model

2.1 Single gap solar cell

Unlike the thermodynamic limits (Landsberg & Tonge, 1980), the limit efficiency considered in the Shockley-Queisser detailed balance model of single-gap solar cell (SGSC) (Shockley & Queisser, 1961) incorporates information on the band structure of the semiconductor and the basic physics. The model includes a number of fundamental assumptions, which allow to evaluate, question and discuss its correctness. All incident photons of energy greater than the energy gap (E_G) of the semiconductor are assumed to participate in the generation of electron-hole pairs. Other assumptions include that no reflection occurs on the surface of the solar cell, the probability of absorption of a photon with energy exceeding the energy gap and creation of electron-hole pair equals one, and so does the probability of collection of the created electron-hole pairs. In the detailed balance model only radiative recombinations between electrons and holes are allowed, by Planck's law proportional to the temperature of the cell. According to this model, all the carriers relax immediately to the band edges in thermal relaxation processes.

The current-voltage equation of the cell under illumination can be written in the following form:

$$J(V) = J_{SC} - J_{Dark}(V), \tag{1}$$

where J_{SC} is the short circuit current, extracted from the cell when its terminals are closed and the load resistance is zero; the short circuit current is independent of the voltage, but depends on the illumination; the dark current J_{Dark} is the current that flows through the p-n

junction under applied voltage, in the case of a solar cell, produced at the terminals of the device under the load resistance R. The detailed balance efficiency is defined as the ratio of the output power P_{out} extracted from the cell to the input power P_{in} of the incident radiation:

$$\eta = \frac{P_{out}}{P_{in}} = \frac{J_m V_m}{P_{in}}, \tag{2}$$

where V_m and J_m is the voltage and current, respectively, that corresponds to the optimal value of the output power.
Both P_{in} and $J(V)$ can be defined in terms of fluxes of absorbed and emitted photons. Let β_s be the incident photon flux, or the number of incident photons per second per square meter received from the sun and the ambient. By Planck's law, describing the blackbody radiation:

$$\beta_s(E) = \frac{2F_s}{h^3c^2} \frac{E^2}{e^{E/k_b T_a} - 1}, \tag{3}$$

where h is the Planck constant, c is the velocity of light, k_b is a Boltzman constant and T_a is a temperature of the ambient. F_s is a geometrical factor determined by the half of the angle subtended by the sunlight:

$$F_s = \pi \sin^2 \frac{\Theta_{sun}}{2}. \tag{4}$$

In all the examples discussed in this chapter the maximum concentration of sunlight, corresponding to $\Theta_{sun} = 180\,^\circ$, is assumed. For that reason there is no need to describe the incident photon flux cming from the ambient and the photon flux described by the equation (3) is the total incident photon flux. The radiation of the sun is coming from all directions. If a flat solar panel receives radiation over a hemisphere, the geometrical factor becomes π, which is equivalent to the cell illuminated with $\Theta_{sun} = 180\,^\circ$.
The input power will be the total energy of all the incident photons:

$$P_{in} = \int_0^\infty E\beta_s(E)\, dE. \tag{5}$$

The short circuit current can be expressed as the elementary charge multiplied by the number of absorbed photons, with the absorption coefficient $a(E)$:

$$J_{SC} = q \int a(E)\beta_s(E)\, dE = q \int_{E_G}^\infty \beta_s(E)\, dE, \tag{6}$$

where the absorption coefficient $a(E)$ (zero for energies lower than the bandgap, one otherwise) determines the lower boundary of the integral.
The dark current is related to the number of photons emitted by the p-n junction:

$$J_{Dark}(V) = q \int e(E)\beta_e(E,V))\, dE, \tag{7}$$

where $e(E)$ is an emission coefficient which describe the probability of the photon emission. The generalized form of Planck's law of blackbody radiation (Landau & Lifshitz, 1980) describes the dependence of the flux β_e of photons emitted by the device on the chemical

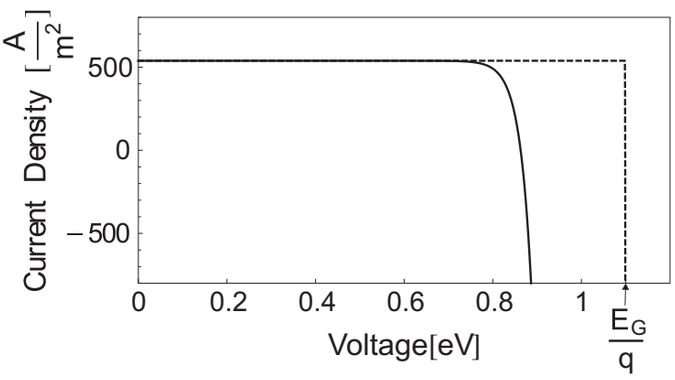

Fig. 2. The current-voltage characteristic of an SGSC with $E_G = 1.1$ eV. The solid and dashed lines represent the $J(V)$ function for a flat cell without concentrators, placed on Earth at a temperature of 300 K and at absolute zero (the temperature corresponding to the ultimate efficiency), respectively.

potential difference, which can be defined by the potential at the terminals:

$$\beta_e(E, \Delta\mu) = \frac{2F_e}{h^3c^2} \frac{E^2}{e^{(E-\Delta\mu)/k_bT_c} - 1}, \tag{8}$$

where T_c is the temperature of the cell, and $\Delta\mu$ is the chemical potential difference defined as the difference of the quasi-Fermi levels (defined in the next Section):

$$\Delta\mu = E_{FC} - E_{FV} = qV. \tag{9}$$

The lower boundary of the integral (7) depends on the emissivity, $e(E)$ (one for energies above E_G, zero otherwise) of the p-n junction, and thus determines the maximum voltage of the junction (the maximum load resistance that can be applied). Above this voltage the device will emit light.
The current-voltage function (1) becomes:

$$J(V) = q \int_{E_G}^{\infty} (\beta_s(E) - \beta_e(E, V))\, dE. \tag{10}$$

Figure 2 presents the current-voltage characteristics of a cell with bandgap E_G at different temperatures. As established above, the maximum voltage (at $T = 0$ K) is determined by E_G. In the limit of $T = 0$ K temperature the value of efficiency achieves its maximum value for the specific solar cell, i.g., the ultimate efficiency.

2.2 Intermediate band solar cells

In this section we will show how to extend the expression (10) to the case of the cell with intermediate band. The model IBSC device, shown in Fig. 3, includes emitters n and p, for separation and extraction of the carriers, and an intermediate band (IB) absorber material placed between them. It is desirable that the IB be thermally separated from the valence band (VB) and the conduction band (CB), so that the number of electrons in the IB can only be changed via photon absorption or emission. This assumption allows to introduce three

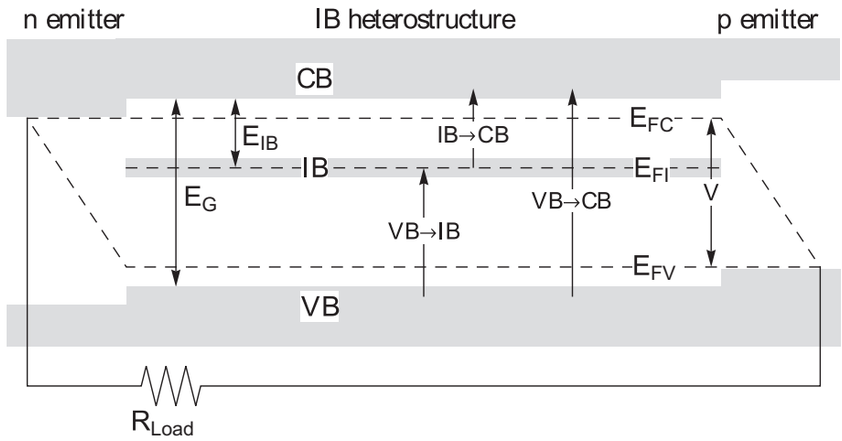

Fig. 3. Model of the band structure of a solar cell with intermediate band. The terminals of the solar cell are connected to the n and p emitters. The possible excitation processes, via one-photon or two-photon absorption, are indicated by arrows. Up down arrows indicate energy differences between band edges.

quasi-Fermi levels, one for each band, to describe the population of electrons within the bands. An infinite mobility of electrons is assumed, to ensure constant quasi-Fermi levels across the junction and minimize the occurrence of non-radiative light traps. The introduction of the IB can improve the efficiency by allowing the absorption of low-energy photons, and thus overcome the problems of the impurity level concept. In Fig. 3 the lowest energy difference between the bands is seen to depend on the value of E_{IB}, the energy difference between the IB and the CB; E_{IB} determines also the threshold energy of the absorbed photons.

In the basic version of the model, the absorption and emission coefficients between each band are assumed to be as presented in Fig. 4. It would probably be more realistic, but still advantageous, to assume that the absorption coefficients corresponding to different transitions are constant, but differ in value. Since the photons that contribute to the transitions between VB and CB predominate in the incident light, the transitions between IB are CB are much weaker that those between VB and IB. According to Martí et al. (2006), the problem has not yet been studied systematically. However, this assumption seems to reflect the behavior of real systems. Thus, the absorption coefficient for different transitions will fulfill the relation:

$$\alpha_{VC} > \alpha_{VI} > \alpha_{IC}. \tag{11}$$

This allows to assume specific values of the absorption coefficients in Fig. 4, but implies that the absorption between IB and CB will be marginal, and so will be the current generated by two-photon absorption.

The assumed form of the absorption and emission functions allows to specify the boundaries of the integrals in the expression for the photon flux absorbed or emitted by the band, analogously to the SGSC model. Three fluxes are distinguished, one for each of the three transitions: VB-CB, VB-IB and IB-CB. Each of the three fluxes contains information on the number of absorbed and emitted photons per unit of time per unit of area:

$$\int_{E_G}^{\infty} \left(\beta_s(E) - \beta_e(E,\mu)\right)\, dE, \tag{12}$$

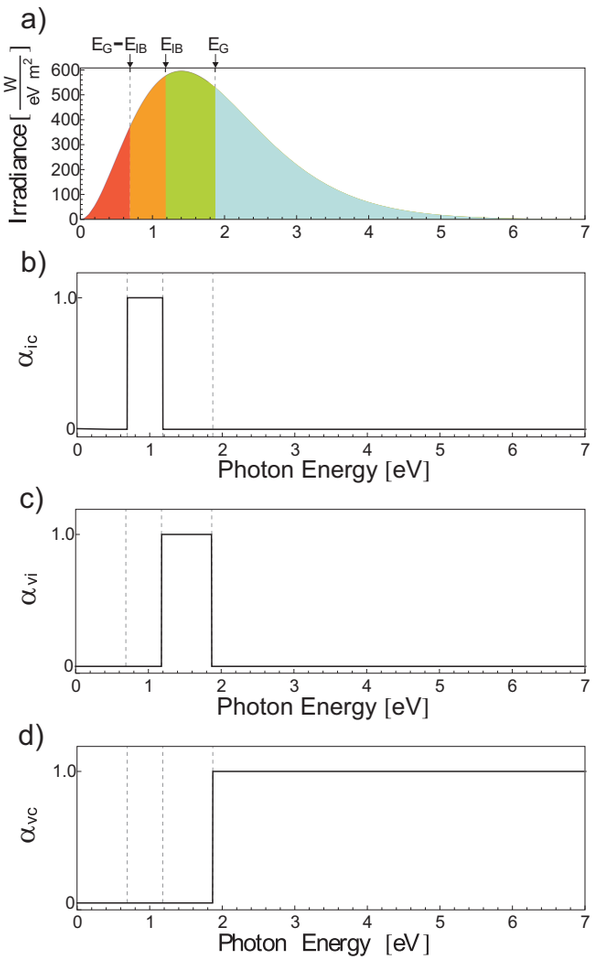

Fig. 4. (a) Radiant emittance of a blackbody at a temperature of 5760 K. Below, plots of the absorption coefficients for (b) IB→CB, (c) VB→IB and (d) VB→CB transitions. The shape of these functions depends on the energy gap and the assumptions made. The depicted forms allow to determine the integral boundaries in equations (12), (13) and (14).

$$\int_{E_G - E_{IB}}^{E_G} \left(\beta_s(E) - \beta_e(E, \mu_1)\right)\, dE, \tag{13}$$

$$\int_{E_{IB}}^{E_G - E_{IB}} \left(\beta_s(E) - \beta_e(E, \mu_2)\right)\, dE, \tag{14}$$

where:

$$\mu_1 = E_{FC} - E_{FI}, \tag{15}$$

$$\mu_2 = E_{FI} - E_{FV}. \tag{16}$$

In the equilibrium state the number of electrons in the IB must be constant, which implies that the increase/decrease due to the VB-IB transition must be equal to the decrease/increase due

to the IB-CB transition:

$$\int_{E_G-E_{IB}}^{E_G} (\beta_s(E) - \beta_e(E,\mu_1))\, dE = \int_{E_{IB}}^{E_G-E_{IB}} (\beta_s(E) - \beta_e(E,\mu_2))\, dE. \tag{17}$$

The separation of the quasi-Fermi levels is determined by the applied load resistance and the voltage produced at the terminals of the solar cell:

$$qV = E_{FC} - E_{FV} = (E_{FC} - E_{FI}) + (E_{FI} - E_{FV}) = \mu_1 + \mu_2. \tag{18}$$

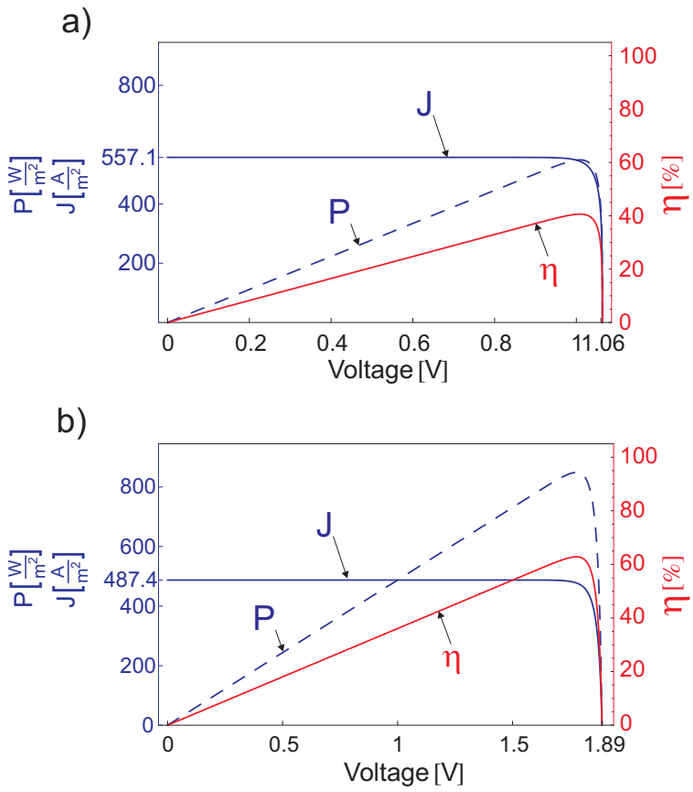

Fig. 5. Voltage dependence of the current density, J, output power P and efficiency η for (a) a single-gap solar cell with $E_G = 1.08$ eV; (b) an intermediate-band solar cell with $E_G = 1.9$ eV, $E_{IB} = 0.69$ eV. The cell has a temperature of 300 K; the incident light is characterized by the blackbody radiation at 5760 K and has a maximum concentration. The band alignment corresponds to the maximum efficiency.

With the last two equations we can calculate the quasi-Fermi level separation for a given voltage (Ekins-Daukees et al., 2005), and thus obtain the current-voltage characteristic. Figure 5 shows the J-V characteristics of (a) an SGSC and (b) an IBSC. The assumed energy gap and intermediate band energy level correspond to the highest possible efficiency of the cell illuminated by sunlight characterized by the 5760 K blackbody radiation, with a maximum concentration. Presented in the same graph, the output power plot shows an increase in efficiency. The short circuit current value is lower in the case of IBSC, but the significant

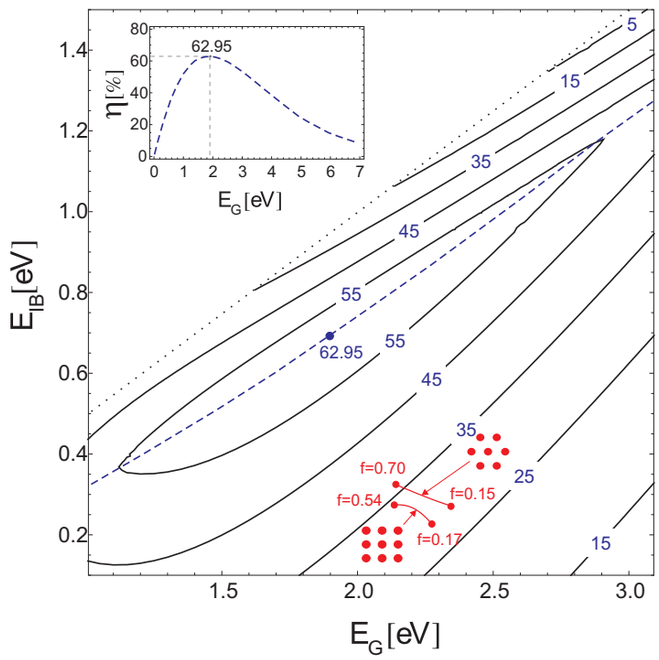

Fig. 6. Contour plot depicting the detailed balance efficiency η versus the energy gap E_G and the distance E_{IB} between the intermediate band bottom and the CB bottom. The values of E_{IB} range from 0 to $\frac{E_G}{2}$. However, according to the model assumed the efficiency is symmetric with respect to E_{IB} in the range from 0 to E_G. the inset in the top-left corner shows the η in dependence on E_G along the dashed line marked in the main figure. The inset shows the changes of E_G, E_I (and η) for AlGaAs supperlattices in dependence on filling fraction (cf. Fig. 11, 12).

increase in the operating voltage leads to a net increase in the efficiency. An explanation of the decrease in the short circuit current in the IBSC (when low-energy photon are absorbed) is provided by Fig. 4, showing the absorption coefficient dependence in the optimal IBSC. The high power absorbed by the cell is seen to contribute to the two-photon processes.
The contour plot in Fig. 6 shows the efficiency versus the bandgap and the distance between IB and CB. These results are important for the understanding of the potential of the IB concept. Later in this chapter they will be compared with simulation data, analyzed in terms of the material parameters used.
If the bandwidth of the solar cell is wider than the distance from the intermediate band to the nearest band, the spectral selectivity might be disturbed. However, these processes are not considered in this chapter. The bandwidth is assumed to only affect the absorption and emission spectra in one of the narrow gaps, changing the boundaries of the integrals in equation (17):

$$\int_{E_G-E_{IB}}^{E_G} (\beta_s(E) - \beta_e(E,\mu_1))\, dE = \int_{E_{IB}-\Delta IB}^{E_G-E_{IB}} (\beta_s(E) - (\beta_e(E,\mu_2))\, dE, \tag{19}$$

where ΔIB is the intermediate band width.

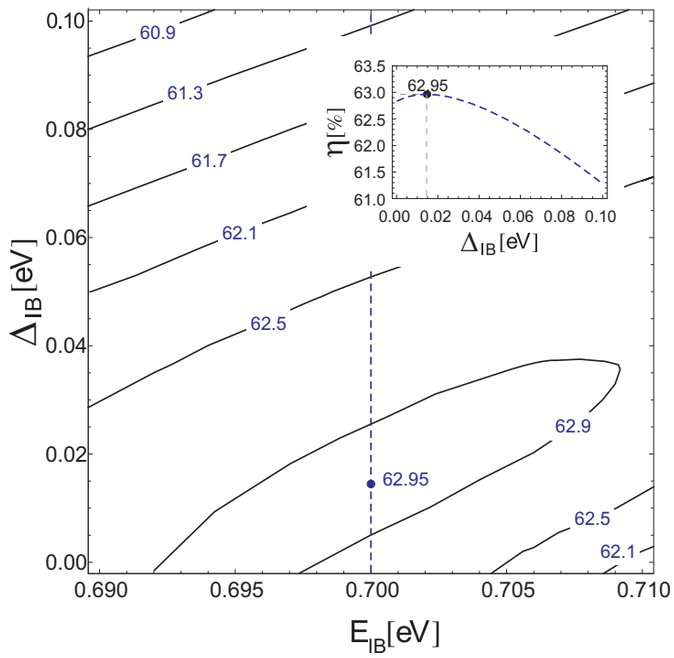

Fig. 7. Detailed balance efficiency of an IBSC with a fixed energy gap $E_G = 1.90$ eV versus the width Δ_{IB} and position E_{IB} of the intermediate band. In the inset, the profile of the efficiency function across the dashed line in the contour plot is shown.

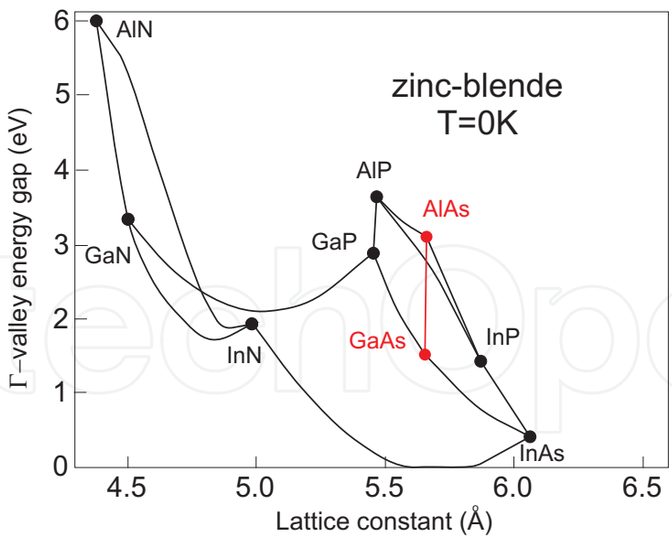

Fig. 8. Energy gap width versus lattice constant for selected III-V group semiconductor compounds. Red line corresponds to the ternary alloy AlGaAs. Note the lattice constant does not change significantly with changing Al concentration in the alloy. (The data have been taken from (Vurgaftman et al., 2001))

In this case an increase in the width of the intermediate band will result in increased absorption, since the gap will shrink. On the other hand, the maximum applicable voltage will decrease with increasing bandwidth, as the emission function will be affected. As shown in Fig. 7, for a fixed energy gap the maximum efficiency may increase. The inset presents the efficiency plotted versus the IB width for energy gap $E_G = 1.90$ eV and intermediate band level $E_{IB} = 0.7$ eV, measured to the top edge of the IB. A maximum is found to occur for $\Delta IB = 0.015$ [eV]; the maximum value is $\eta = 62.96\%$. An improvement by 0.04% is reported in (Green, 2003). An increase by 0.03% is achieved in the cell illuminated by the 6000 K blackbody radiation for $\Delta IB = 0.02$ eV.

3. Calculation of the band structure

We consider a 2D semiconductor superlattice which consists of a periodic array of semiconductor inclusions embedded in a semiconductor matrix. Such a system has an artificially introduced periodicity with a lattice constant much larger than the interatomic distances. As a result of introducing this additional periodicity the conduction and valence bands split into a set of minibands. In this regime of length and energy we can regard the system as continuous on the atomic scale and, in the case of direct gap semiconductors, use the effective parameters describing the position and curvature of the conduction band bottom and the valence band top. Then, the miniband structure of the conduction and valence bands can be calculated with the aid of effective Hamiltonians with spatially dependent effective parameters (Bastart, 1988; Burt, 1999; Califano & Harison, 2000). In the case of semiconductors with a relatively wide gap, such as AlGaAs, the electronic system can be decoupled from the system of light and heavy holes. Also, the stress at the inclusion/matrix interfaces can be neglected in materials of this kind, because of the small atomic lattice constant changes related to the different concentration of Al in the alloy (see Fig. 8). Thus, the simple BenDaniel-Duke Hamiltonian (BenDaniel & Duke, 1966) can be used for electrons in the vicinity of point Γ of the solid semiconductor structure:

$$\left[-\alpha\left(\frac{\partial}{\partial x}\frac{1}{m^*(\boldsymbol{r})}\frac{\partial}{\partial x}+\frac{\partial}{\partial y}\frac{1}{m^*(\boldsymbol{r})}\frac{\partial}{\partial y}+\frac{\partial}{\partial z}\frac{1}{m^*(\boldsymbol{r})}\frac{\partial}{\partial z}\right)+E_C(\boldsymbol{r})\right]\Psi_e(\boldsymbol{r})=E\Psi_e(\boldsymbol{r}), \tag{20}$$

where $\boldsymbol{r}$ is the position vector in 3D space. The dimensionless constant $\alpha = 10^{-20}\hbar^2/(2m_e e) \approx 3.80998$ (m_e and e are the free electron mass and charge, respectively) allows to express the energy and the spatial coordinates in eV and Å, respectively; m^* is the effective mass of the electron; E_C denotes the conduction band bottom. Both parameters are periodic with the superlattice period:

$$\begin{aligned} m^*(\mathbf{r}+\mathbf{R}) &= m^*(\mathbf{r}),\\ E_C(\mathbf{r}+\mathbf{R}) &= E_C(\mathbf{r}), \end{aligned} \tag{21}$$

where $\boldsymbol{R}$ is a lattice vector of the superlattice. We have used the following empirical formulae for a linear extrapolation of the material parameter values in GaAs and AlAs to estimate their values in the $Al_xGa_{1-x}As$ matrix: $E_C = 0.944x$ and $m^* = 0.067 + 0.083x$, x is a concentration of the Al in GaAs (Shanabrook et al., 1989; Vurgaftman et al., 2001).

In the case of a zinc blende structure (e.g., AlGaAs) both the light- and heavy-hole bands must be taken into account. The Schrödniger equation for each component of the envelope function

for light-holes, Ψ_{lh} and heavy-holes Ψ_{hh} reads (Datta, 2005):

$$-\begin{pmatrix} \hat{P}+\hat{Q} & 0 & -\hat{S} & \hat{R} \\ 0 & \hat{P}+\hat{Q} & \hat{R}^* & \hat{S}^* \\ -\hat{S}^* & \hat{R} & \hat{P}-\hat{Q} & 0 \\ \hat{R}^* & \hat{S} & 0 & \hat{P}-\hat{Q} \end{pmatrix} \mathbf{\Psi}_h(\boldsymbol{r}) = E\mathbf{\Psi}_h(\boldsymbol{r}), \tag{22}$$

where

$$\mathbf{\Psi}_h(\boldsymbol{r}) = \left(\Psi_{lh\uparrow}(\boldsymbol{r}), \Psi_{lh\downarrow}(\boldsymbol{r}), \Psi_{hh\downarrow}(\boldsymbol{r}), \Psi_{hh\uparrow}(\boldsymbol{r}) \right)^T. \tag{23}$$

The subscripts *lh* and *hh* label the components of the envelope function for the light and heavy holes, respectively. The symbols $\uparrow$ and $\downarrow$ refer to bands related to opposite z components of the light- and heavy-hole spins. The operators $\hat{P}$, $\hat{Q}$, $\hat{R}$ and $\hat{S}$ have the form:

$$\begin{aligned}
\hat{P} &= E_V(\boldsymbol{r}) + \alpha \left(\frac{\partial}{\partial x}\gamma_1(\boldsymbol{r})\frac{\partial}{\partial x} + \frac{\partial}{\partial y}\gamma_1(\boldsymbol{r})\frac{\partial}{\partial y} + \frac{\partial}{\partial z}\gamma_1(\boldsymbol{r})\frac{\partial}{\partial z} \right), \\
\hat{Q} &= \alpha \left(\frac{\partial}{\partial x}\gamma_2(\boldsymbol{r})\frac{\partial}{\partial x} + \frac{\partial}{\partial y}\gamma_2(\boldsymbol{r})\frac{\partial}{\partial y} - 2\frac{\partial}{\partial z}\gamma_2(\boldsymbol{r})\frac{\partial}{\partial z} \right), \\
\hat{R} &= \alpha\sqrt{3} \left[-\left(\frac{\partial}{\partial x}\gamma_2(\boldsymbol{r})\frac{\partial}{\partial x} - \frac{\partial}{\partial y}\gamma_2(\boldsymbol{r})\frac{\partial}{\partial y} \right) + i\left(\frac{\partial}{\partial x}\gamma_3(\boldsymbol{r})\frac{\partial}{\partial y} + \frac{\partial}{\partial y}\gamma_3(\boldsymbol{r})\frac{\partial}{\partial x} \right) \right], \\
\hat{S} &= \alpha\sqrt{3} \left[\left(\frac{\partial}{\partial x}\gamma_3(\boldsymbol{r})\frac{\partial}{\partial z} + \frac{\partial}{\partial z}\gamma_3(\boldsymbol{r})\frac{\partial}{\partial x} \right) - i\left(\frac{\partial}{\partial y}\gamma_3(\boldsymbol{r})\frac{\partial}{\partial z} + \frac{\partial}{\partial z}\gamma_3(\boldsymbol{r})\frac{\partial}{\partial y} \right) \right].
\end{aligned} \tag{24}$$

The Luttinger parameters γ_1, γ_2, γ_3, describe, the effective masses $1/(\gamma_1+\gamma_2)$ and $1/(\gamma_1-\gamma_2)$ of light and heavy holes near point Γ of the atomic lattice are, like the position of the valence band top E_V, periodic in the superlattice structure:

$$\begin{aligned}
\gamma_\beta(\mathbf{r}+\mathbf{R}) &= \gamma_\beta(\mathbf{r}), \\
E_V(\mathbf{r}+\mathbf{R}) &= E_V(\mathbf{r}),
\end{aligned} \tag{25}$$

where the subscript β is 1, 2 or 3. For periodic heterostructures consisting of a triangular or square lattice-based system of GaAs rods embedded in $Al_xGa_{1-x}As$, the following material parameter values, dependent on the concentration of Al in aluminium gallium arsenide, can be assumed (Shanabrook et al., 1989; Vurgaftman et al., 2001):

$$\begin{aligned}
E_V &= 1.519 + 0.75x, \\
\gamma_1 &= 6.85 - 3.40x, \\
\gamma_2 &= 2.10 - 1.42x, \\
\gamma_3 &= 2.90 - 1.61x.
\end{aligned} \tag{26}$$

We are interested in the calculation of the spectra of a finite-thickness periodic layer of inclusions (see Fig. 9). In such superlattices, when the superlattice period and the layer thickness are of the order of a few nanometers the lowest miniband within the CB is detached from the other CB minibands. Moreover, the higher CB minibands overlap to form a continuous energy range without minigaps.

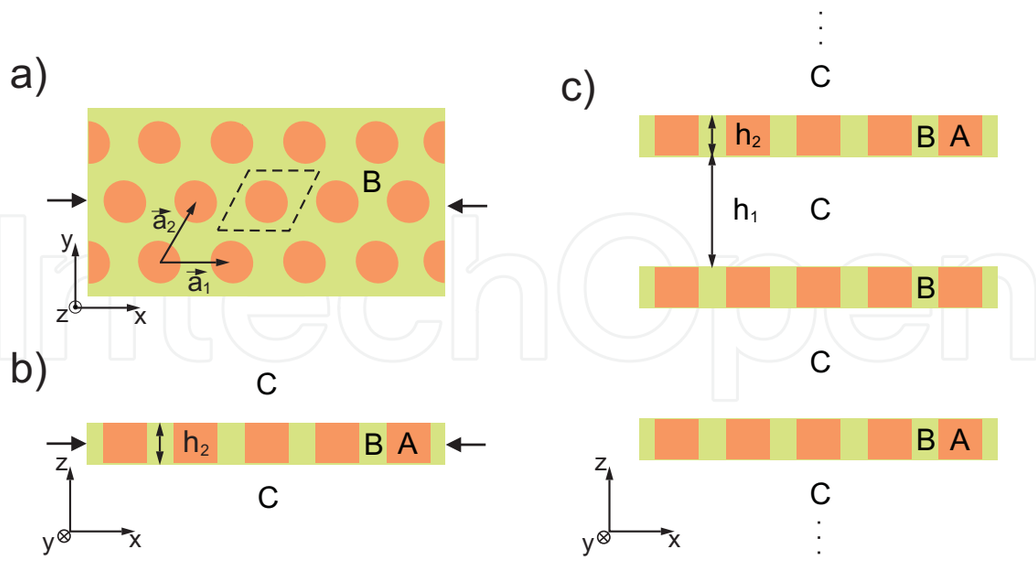

Fig. 9. Structure of a periodic slab with inclusions in triangular lattice, (a) top and (b) side view. Letters A, B and C denote the inclusion, matrix and spacer materials, respectively. The arrows indicate the cross-section plane. Dashed parallelogram in (a) delimits the unit cell, which reproduces the whole plane when translated by superlattice vectors $\boldsymbol{a}_1$ and $\boldsymbol{a}_1$. (c) The supercell structure used in the plane wave method: an infinite stack of replicas of the periodic slab.

In the VB all the minibands overlap or are separated by extremely narrow minigaps. Let us assume for simplicity that the total spectrum can by approximated by the model with a single gap (delimited by the top of the highest VB miniband and the bottom of the block of higher CB minibands) and a single intermediate band formed by the first (lowest) CB miniband.
This simplification allows us to calculate the detailed balance efficiency of solar energy conversion for a superlattice-based solar cell using the model with a single intermediate band within the gap.

3.1 Plane wave method

We have calculated the band structure of electrons and holes by the plane wave method (PWM), a technique successfully applied to studying the electronic states in semiconductor heterostructures with quantum dots and wires of different shape and size, as well as interdiffusion and strain effects on electronic bands (Cusack et al., 1996; Gershoni et al., 1988; Li & Zhu, 1998; Li et al., 2005; Ngo et al., 2006; Tkach et al., 2000). By Fourier-expanding the spatially dependent structural parameters: m^*, γ_β, E_C, E_V, and the electron and hole envelope functions the differential equations (20) and (22) can be transformed to a set of algebraic equations for the Fourier coefficients of the envelope functions. This set of equations has the form of an eigenvalue problem with eigenvalues being the energies of successive minibands for the selected wave vector.
The PWM can only be applied to periodic systems. The structure under consideration is finite in one direction, though. To adopt the method to the case considered we calculate the spectrum of an infinite stack of weakly coupled periodic layers, as presented in Fig. 9(c). If

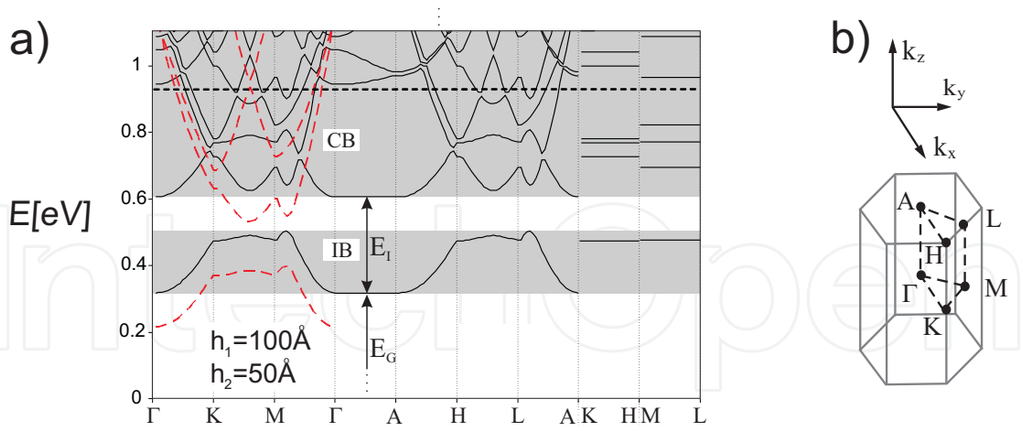

Fig. 10. (a) Electronic minibands in the structure presented in Fig. 9, with GaAs cylinders (material A) embedded in $Al_{0.35}Ga_{0.65}As$ slabs (B) separated by an AlAs spacer (C). Red dashed line represents bands in a 2D superlattice formed by an array of infinitely long rods (i.e., for $k_z = 0$). For a sufficiently thick spacer layer the minigaps are dispersionless in the z direction (lines K-H and M-L in the Brillouin zone shown in (b)). This proves a good separation of the periodic slabs. The calculations were performed for a superlattice with lattice constant a = 50 Å and filling fraction $f = 0.3$. The reference energy level $E = 0$ eV corresponds to the CB bottom in solid GaAs. The slab thickness h_2 is 50 Å and the AlAs spacer thickness h_1 is 100 Å.

the distance between adjacent layers is large and the potential in the spacer material C forms a high barrier both for electrons and holes, the spectrum of the system is very close to that of a single isolated layer (Rodríguez-Bolívar et al., 2011).
Figure 10(a) shows the electronic spectrum of the structure presented in Fig. 9, with circular GaAs rods embedded in AlGaAs slabs. Adjacent GaAs/AlGaAs slabs are separated by an AlAs spacer, relatively thick and with a high potential to ensure a good separation of the periodic slabs. This is reflected in the flat dispersion in the z direction (high-symmetry lines K-H, M-L, Γ-A) and the repeated shape of the dispersion branches $\Gamma - K - M - \Gamma$ and $A - H - L - A$. Thus, the case considered proves equivalent to that of a single periodic slab. In the considered range of structural parameter values the electronic spectrum includes one clearly detached miniband and a continuous block of minibands above it. The VB minibands (not shown in Fig. 10) overlap. Thus, the model with a single intermediate band (formed by the first CB miniband) within the energy gap (between the VB and the block of CB minibands) can be used for the calculation of the detailed balance efficiency.

4. Detailed balance efficiency of periodic semiconductor slab

We calculate the electronic and hole spectra of periodic semiconductor layers with different filling fraction values. The filling fraction is defined as the ratio of the in-plane cross-section S_{inc} of the inclusion to the area S of the unit cell area:

$$f = \frac{S_{inc}}{S}. \tag{27}$$

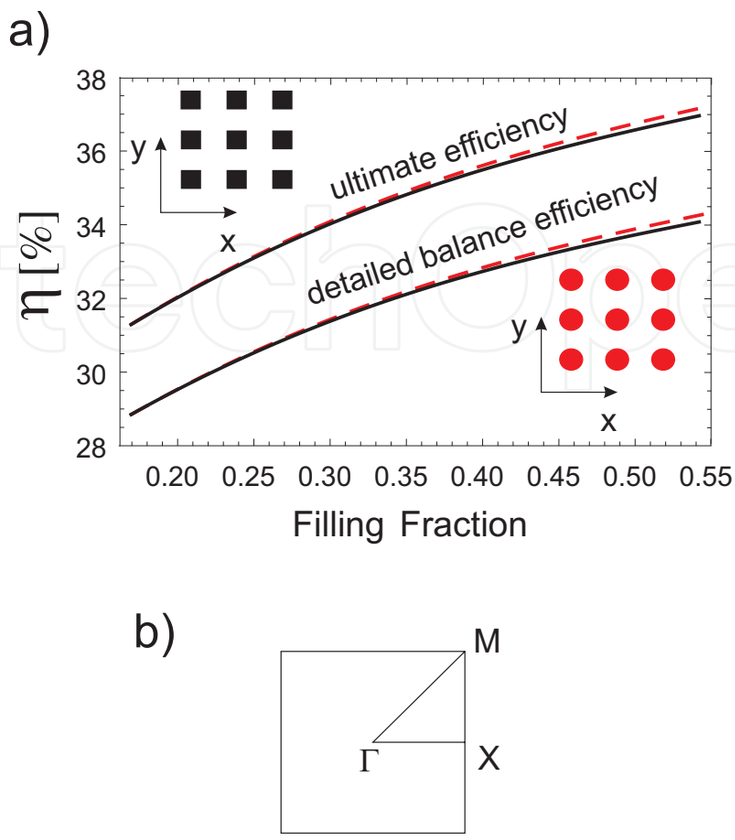

Fig. 11. (a) Detailed balance efficiency and ultimate efficiency of solar energy conversion versus filling fraction for a slab (of thickness h_2=50Å) with cylinders (dashed red line) and square prisms (solid black line) arranged in a square lattice (the lattice constant of the superlattice is $a = 50$ Å). The inclusion, slab and spacer materials are GaAs, $Al_{0.35}Ga_{0.65}As$ and AlAs, respectively. (b) The high-symmetry line in the first Brillouin zone used in the search of absolute minigaps.

We consider two shapes of the inclusions: cylinders and square prisms, and two lattices: the square and triangular lattice. Thus, four combinations of the system geometry are possible. For each combination we calculate the position and width of the valence and conduction bands versus the filling fraction. The following parameters of the band structure are extracted from the calculations:

- the width of the energy gap E_G between the top of the VB and the bottom of the block of CB minibands,
- the shift E_I between the bottom of the first CB miniband and the bottom of the block of higher CB minibands,
- the width ΔE_I of the intermediate band (the first CB miniband).

All three parameters are used in the calculation of the detailed balance efficiency of solar energy conversion for four geometries mentioned above.

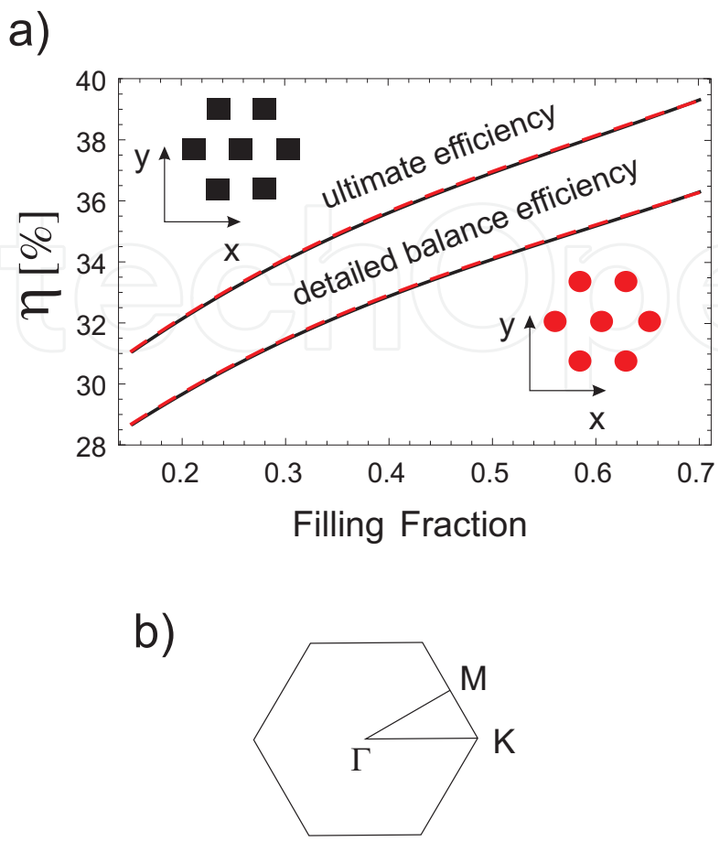

Fig. 12. (a) Detailed balance efficiency and ultimate efficiency of solar energy conversion versus filling fraction for a slab (of thickness h_2=50Å) with cylinders (dashed red line) and square prisms (solid black line) arranged in a triangular lattice (the lattice constant of the superlattice is $a = 50$ Å). The inclusion, slab and spacer materials are GaAs, $Al_{0.35}Ga_{0.65}As$ and AlAs, respectively. (b) The high-symmetry line in the first Brillouin zone used in the search of absolute minigaps.

The lattice constant of the superlattice is fixed at $a = 50$ Å. The assumed thickness of the periodic slab is $h_2 = 50$ Å. A maximum efficiency can be observed in this size range, with the thickness of the periodic slab comparable to the lattice constant of the superlattice. The inclusion and matrix materials are GaAs and $Al_{0.35}Ga_{0.65}As$, respectively. A thick AlAs spacer (of thickness $h_1 = 100$Å) ensures a good separation of adjacent periodic slabs in the PWM supercell calculations. We used $15x15x15$ and $13x13x13$ plane waves in the calculations of the electronic and hole spectra, respectively.

Figures 11(a) and 12(a) present the calculated ultimate efficiency and detailed balance efficiency versus filling fraction. To investigate the width of the absolute minibands/minigaps we calculated the electronic and hole spectra along the high-symmetry lines shown in Figs.11(b) and 12(b) for square and triangular lattices. The assumed upper bound of ≈ 0.7 of the filling fraction range in Fig. 12 (triangular lattice) corresponds to the maximum filling fraction values, or touching adjacent inclusions, in the considered structures: 0.68 for

cylindrical inclusions and 0.86 for inclusions in the shape of square prism. The upper limit of filling fraction for square lattice $\approx$ 0.55 in Fig. 11 results form minibands crossing (and disappearing of the minigap between the lowest conduction miniband and the rest of the minibands in CB) for higher values of f. The lower limit of the filling fraction, $f = 0.15$, is assumed for accuracy of the results obtained by the PWM. A good convergence of results is achieved for intermediate filling fraction values (far from 0 and 1).

The shape of the inclusions is seen to play no important role as long as the filling fraction value is kept. This is evidenced by the overlapping of the solid black and dashed red lines, referring to structures with square prisms and cylinders, respectively, in Figs. 11 and 12. Only in the square lattice case, a minor difference in the efficiency is seen to occur due to the inclusion shape in the range of larger filling fraction values.

Crucial for the efficiency are the lattice symmetry and the filling fraction. In the considered structures the efficiency tends to be higher in the case of the triangular lattice. The maximum values of ultimate (detailed balance) efficiency, 39.5% (35.5%) for the triangular lattice, are reached for large filling fraction values, corresponding to inclusions getting in touch. For this lattice type the efficiency grows monotonically with increasing filling fraction. In the case of the square lattice the filling fraction dependence of the ultimate (detailed balance) efficiency has a maximum of 37% (34%) for filling fraction value $f \approx 0.55$ for which the band crossing appears. For both lattice types the efficiency changes more rapidly in the range of low filling fraction values.

The change of filling fraction affects on the band structure and the values of E_G and E_I parameters which determine the efficiency of solar energy conversion in the supperlatice based solar cell. In the inset in Fig. 6 the detailed balance efficiency as a function of E_G and E_I was plotted (see the curves marked in red) for considered structures. We showed the results for systems with circular inclusions only because the week dependence of η on the inclusion shape. One can notice that the structure (or material) more suitable for solar cell application than the considers supperlattices has to poses slightly smaller energy gap E_G and much bigger separation between IB and CB, E_I. It is evident (see Fig. 8) that materials with better values of the energy gap can be chosen, e.g., InAs/GaAs (Jolley et al., 2010; Zhou et al., 2010) where the lattice mismatch between compounds induces stress which modify the band structure (39% detailed balance efficiency is predicted (Tomić, 2010), other compounds form III-V group ($InAs/Al_xGa_{1-x}As$, $InAs_{1-x}N_y/AlAs_xSb_{1-x}$, and $InAs_{1-z}N_z/Al_x[Ga_yIn_{1-y}]_{1-x}P$) where 60% detailed balance efficiency at maximum gap concentration where recently calculated (Linares et al., 2011).

5. Experiments

One of the first important experiments related directly to the concept of IBSC was the study by Luque et al. (2005), in which two main operating principles required from the IBSC (the production of photocurrent from photons of energy below the bandgap and the occurrence of three separate quasi-Fermi levels) were confirmed by measurements of quantum efficiency and electroluminescence. In the paper Martí et al. (2006) claim they demonstrate for the first time the production of photocurrent with a simultaneous absorption of two sub-bandgap energy photons, and prove the possibility of obtaining the photocurrent by two-photon absorption processes in InAs/(Al,Ga)As quantum dot (QD) structures.

Although the first experiments prove the possibility of photocurrent production by two-photon absorption, many obstacles still prevent the achievement of satisfactory performance. In another study, Martí et al. (2007) demonstrate that strain-induced dislocations can propagate from the QD region to the p emitter, resulting in a decrease in the minority carrier lifetime and, consequently, reducing the efficiency. Most of the conclusions drawn from the recent experiments point out the common problem of decrease in open-circuit voltage. These effects are investigated in Jolley et al. (2010).

6. Conclusions

We have examined thoroughly the effect of the (super)lattice symmetry and the cross-sectional shape of the rods on the efficiency of the solar cells based on thin slabs of quantum wire arrays by comparing structures consisting of GaAs cylinders or square prisms, embedded in $Al_xGa_{1-x}As$ and disposed in sites of square or triangular lattice. We show the gain in efficiency of semiconductor slabs with 2D periodicity in comparison with the efficiency of monolithic semiconductors (with a single bandgap). The key role in the gain of efficiency is played by the lowest conduction miniband, which, detached from the overlapping conduction minibands, acts as an intermediate band that opens an extra channel for carrier transitions between the valence band and the conduction band. Another parameter of vital importance for the efficiency of solar-energy conversion is the distance between the top of the highest valence miniband and the bottom of the overlapping conduction minibands. This distance, determines the energy of utilized carriers. Even though the obtained values of the width of the minigap are not optimal to obtain maximal efficiency (Bremner et al., 2009; Luque & Martí, 1997; Shao et al., 2007), the increase in efficiency is significant as compared to the bulk solar cells (Kłos & Krawczyk, 2009). The impact of the discretisation of the valence band on the efficiency of the photovoltaic effect is be much lesser than that of the discretisation of the conduction band, and, in the first approximation, can be regarded as limited to a shift in valence band top in the evaluation of solar cell efficiency (Kłos & Krawczyk, 2009).

7. References

Araujo, G. L. & Martí, A., (1995). Electroluminescence coupling in multiple quantum well diodes and solar cells, *Appl. Phys. Lett.* Vol. 66: 894Ű895.

Ashcroft, N. W. & Mermin, D. N., (1976) *Solid State Physics*, Saunders Collage Publishing.

Barnham, K. W. J. & Duggan, G., (1990). A new approach to high-efficiency multi-band-gap solar cells, *J. Appl. Phys.* Vol. 67: 3490-3493.

Bastard, G. (1988). *Wave Mechanics Applied to Semiconductor Heterostructures*, Les editions de Physique, Paris.

BenDaniel, D. J. & Duke, C. B. (1966). Space-charge effects on electron tunneling, *Phys. Rev.* Vol. 152: 683-692.

Bremner, S. P., Levy, M. Y. & Honsberg, C.B. (2009). Limiting efficiency of an intermediate band solar cell under a terrestrial spectrum, *Appl. Phys. Lett.* Vol. 92: 171110-1-3.

Burt, M.G. (1999). Fundamentals of envelope function theory for electronic states and photonic modes in nanostructures, *J. Phys.: Condens. Matter* Vol. 11, R53-R83.

Califano, M. & Harison, P. (2000). Presentation and experimental validation of a single-band, constant-potential model for self-assembled InAs/GaAs quantum dots, *Phys. Rev. B* Vol. 61: 10959-10965.

Cusack, M. A., Briddon, P. R. & Jaros, M. (1996). Electronic structure of InAs/GaAs self-assembled quantum dots, *Phys. Rev. B* Vol. 54: R2300-R2303.

Datta, S. (2005). *Quantum Transport: Atom to Transistor*, Cambridge University Press, Cambridge.

Ekins-Daukes, N. J., Honsberg, C. B. & Yamaguchi M., (2005). Signature of intermediate band materials from luminescence measurements, *Presented at the 31st IEEE Photovoltaic Specialists Conference*.

Gershoni, D., Temkin, H., Dolan, G. J., Dunsmuir, J., Chu, S. N. G. & Panish, M. B. (1988). Effects of two-dimensional confinement on the optical properties of InGaAs/InP quantum wire structures, *Appl. Phys. Lett.* Vol. 53: 995-997.

Green, M. A. (2003). *Third Generation Photovoltaics: Advanced Solar Energy Conversion*, Springer-Verlag, Berlin.

Guettler, G. & Queisser, H. J. (1970). Impurity photovoltaic effect in silicon, *Energy. Conversion* Vol. 10(2): 51-5.

Jolley, G., Lu, H. F., Fu, L., Tan, H. H. & Jagadish, C. (2010). Electron-hole recombination properties of $In_{0.5}Ga_{0.5}As$/GaAs quantum dot solar cells and the influence on the open circuit voltage, *Appl. Phys. Lett.* Vol. 97: 123505-1-3.

Keevers, M.J. & Green, M.A., (1994). Efficiency improvements of silicon solar cells by the impurity photovoltaic effect, *J. Appl. Phys.* Vol. 75: 4022-4031.

Kłos, J. W. & Krawczyk, M., (2009). Two-dimensional GaAs/AlGaAs superlattice structures for solar cell applications: Ultimate efficiency estimation, *J. Appl. Phys.* Vol. 106: 093703-1-9.

Kłos, J. W. & Krawczyk, M., (2010). Electronic and hole spectra of layered systems of cylindrical rod arrays: aolar cell application, *J. Appl. Phys.* Vol. 107: 043706-1-5.

Krawczyk, M. & Kłos, J. W., (2010). Electronic and hole minibands in quantum wire arrays of different crystallographic structure, *Physics Letters A* Vol. 374: 647-654.

Landau, L.D. & Lifshitz, E.M., (1980). *Statistical Physics*, Part 1. Vol. 5 (3rd ed.). Butterworth-Heinemann.

Landsberg, P. T. & Tonge, G. (1980). Thermodynamic energy conversion efficiencies, *J. Appl. Phys.* 51: R1-R20.

Li, S.-S. & Zhu, B.-F. (1998). Electronic structures of GaAs/AlAs lateral superlattices, *J. Phys.: Condend. Matter* Vol. 10: 6311-6319.

Li, S.-S., Chang, K. & Xia, J.-B. (2005). Effective-mass theory for hierarchical self-assembly of GaAs/$Al_xGa_{1-x}As$ quantum dots, *Phys. Rev. B* Vol. 71: 155301-1-7.

Lin, A. S., Wang, W. & Phillips, J. D., (2009). Model for intermediate band solar cells incorporating carrier transporta and recombination, *J. Appl. Phys.* Vol. 105: 064512-1-8.

Linares, P. G., Martí, A., Antolín, E. & Luque , A. (2011). III-V compound semiconductor screening for implementing quantum dot intermediate band solar cells, *J. Appl. Phys.* Vol. 109: 014313-1-8.

López, N., Reichertz, L. A., Yu, K. M., Campman, K. & Walukiewicz, W. (2011). Engineering the electronic band structure for multiband solar cells, *Phys. Rev. Lett.* Vol. 106: 028701-1-4.

Luque, A. & Martí, A. (1997). Increasing the efficiency of ideal solar cells by photon induced transitions at intermediate levels, *Phys. Rev. Lett* Vol. 78: 5014-5018.

Luque, A. & Martí, A., (2001). A metallic intermediate band high efficiency solar cell, *Prog. Photovolt. Res. Appl.* Vol. 9(2): 73-86.

Luque, A., Martí, A., López, N., Antolín, E., Cánovas, E., Stanley, C., Farmer, C., Caballero, L. J., Cuadra, L. & Balenzategui, J. L., (2005). Experimental analysis of the quasi-Fermi level split in quantum dot intermediate-band solar cells, *Appl. Phys. Lett.* Vol. 87: 083505-1-3.

Luque, A. & Martí, A., (2011). Towards the intermediate band, *Nature Photonics* Vol. 5: 137-138.

Martí, A., López, N., Antolín, E., Cánovas, E., Stanley, C., Farmer, C., Cuadra, L. & Luque, A., (2006). Novel semiconductor solar cell structures: The quantum dot intermediate band solar cell, *Thin Solid Films* Vol. 511-512: 638-644.

Martí, A., Antolín, E., Stanley, C., Farmer, C., López, N., Díaz, P., Cánovas, E., Linares, P. G. & Luque, A., (2006). Production of photocurrent due to intermediate-to-conduction-band transitions: a demonstration of a key operating principle of the intermediate-band solar cell, *Phys. Rev. Lett.* Vol. 97: 247701-1-4.

Martí, A., López, N., Antolín, E., Cánovas, E., Luque, A., Stanley, C., Farmer, C. & Díaz, P., (2007). Emitter degradation in quantum dot intermediate band solar cells, *Appl. Phys. Lett.* Vol. 90: 233510-1-3.

Messenger, R. A. & Ventre, J. (2004). *Photovoltaic Systems Engineering*, CRC Press, Florida.

Navruz, T. S. & Saritas, M., (2008). Efficiency variation of the intermediate band solar cell due to the overlap between absorption coefficients, *Solar Energy Materials & Solar Cells* Vol. 92: 273-282

Nelson, J. (2003). *The Physics of Solar Cells*, Imperial College, UK.

Ngo, C. Y., Yoon, S. F., Fan, W. J. & Chua, S. J. (2006). Effects of size and shape on electronic states of quantum dots, *Phys. Rev. B* Vol. 74: 245331-1-10.

Rodríguez-Bolívar, S., Gómez-Campos, F. M., Luque-Rodríguez, A., López-Villanueva, J. A., Jiménez-Tejada, J. A. & Carceller, J. E. (2011). Miniband structure and photon absorption in regimented quantum dot systems, *J. Appl. Phys.* Vol. 109: 074303-1-7.

Shanabrook, B. V., Glembocki, O. J., Broido, D. A. & Wang, W. I. (1989). Luttinger parameters for GaAs determined from the intersubband transitions in GaAs/$Al_xGa_{1-x}As$ multiple quantum wells, *Phys. Rev. B* Vol. 39: 3411-3414.

Shao, Q., Balandin, A. A., Fedoseyev, A. I. & Turowski, M. (2007). Intermediate-band solar cells based on quantum dot supracrystals, *Appl. Phys. Lett.* Vol. 91: 163503-1-3.

Shockley, W. & Queisser, H. J. (1961). Detailed balance limit of efficiency of p-n junction solar cells, *J. Appl. Phys.* Vol. 32, 510-519.

Tkach, N. V., Makhanets, A. M. & Zegrya, G. G. (2000). Energy spectrum of electron in quasiplane superlattice of cylindrical quantum dots, *Semicond. Sci. Technol.* Vol. 15: 395-398.

Tomić, S. (2010). Intermediate-band solar cells: Influence of band formation on dynamical processes in InAs/GaAs quantum dot arrays, *Phys. Rev. B* Vol. 82: 195321-1-15.

Vurgaftman, I., Meyer, J. R. & Ram-Mohan, L. R. (2001). Band parameters for III-V compound semiconductors and their alloys, *J. Appl. Phys.* Vol. 89: 5815-5875.

Wolf, M. (1960). Limitations and possibilities for improvements of photovoltaic solar energy converters, *Proc. IRE* Vol. 48: 1246-1263.

Würfel, P. (1993). Limiting efficiency for solar cells with defects from a three-level model, *Sol. Energy Mater. Sol. Cells* Vol. 29: 403-413.

Zhou, D., Sharma, G., Thomassen, S. F., Reenaas, T. W. & Fimland, B. O. (2010). Optimization towards high density quantum dots for intermediate band solar cells grown by molecular beam epitaxy, *Appl. Phys. Lett.* Vol. 96: 061913-1-3.

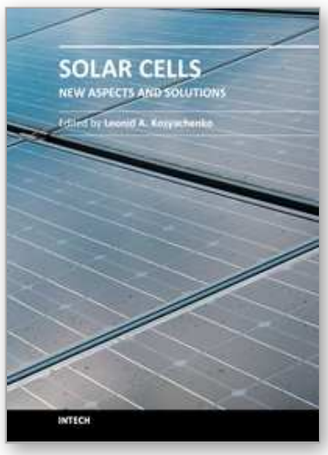

Solar Cells - New Aspects and Solutions

Edited by Prof. Leonid A. Kosyachenko

ISBN 978-953-307-761-1
Hard cover, 512 pages
Publisher InTech
Published online 02, November, 2011
Published in print edition November, 2011

The fourth book of the four-volume edition of 'Solar cells' consists chapters that are general in nature and not related specifically to the so-called photovoltaic generations, novel scientific ideas and technical solutions, which has not properly approved. General issues of the efficiency of solar cell and through hydrogen production in photoelectrochemical solar cell are discussed. Considerable attention is paid to the quantum-size effects in solar cells both in general and on specific examples of super-lattices, quantum dots, etc. New materials, such as cuprous oxide as an active material for solar cells, AlSb for use as an absorber layer in p-i-n junction solar cells, InGaAsN as a promising material for multi-junction tandem solar cells, InP in solar cells with MIS structures are discussed. Several chapters are devoted to the analysis of both status and perspective of organic photovoltaics such as polymer/fullerene solar cells, poly(p-phenylene-vinylene) derivatives, photovoltaic textiles, photovoltaic fibers, etc.

INTECH
open science | open minds

InTech Europe
University Campus STeP Ri
Slavka Krautzeka 83/A
51000 Rijeka, Croatia
Phone: +385 (51) 770 447
Fax: +385 (51) 686 166
www.intechopen.com

InTech China
Unit 405, Office Block, Hotel Equatorial Shanghai
No.65, Yan An Road (West), Shanghai, 200040, China
中国上海市延安西路65号上海国际贵都大饭店办公楼405单元
Phone: +86-21-62489820
Fax: +86-21-62489821

IntechOpen